Research Article | Vol. 9, No. 3 | 1 Mar 2019 | OPTICAL MATERIALS EXPRESS 1062
Optical Materials EXPRESS

Enhanced red emissions and higher quenching temperature based on the intervalence charge transfer in Pr^{3+} doped $LiNbO_3$ with Mg^{2+} incorporation

S. W. LONG,[1,2] M. M. YANG,[2,4] D. C. MA,[3] Y. Z. ZHU,[3] S. P. LIN,[3,5] AND B. WANG[1,2,3,6]

[1]School of Physics, Sun Yat-sen University, Guangzhou 510275, China
[2]State Key Laboratory of Optoelectronic Materials and Technologies, Sun Yat-sen University, Guangzhou 510275, China
[3]Sino-French Institute of Nuclear Engineering and Technology, Sun Yat-sen University, Zhuhai, 519082, China
[4]School of Materials Science and Engineering, Sun Yat-sen University, Guangzhou 510275, China
[5]lshpeng@mail.sysu.edu.cn
[6]wangbiao@mail.sysu.edu.cn

Abstract: For investigating the effect of exceeding Mg^{2+} doping on optical properties and luminescent mechanism, detailed spectroscopic characterizations of Pr^{3+} (1 mol%) and Mg^{2+} (0 and 5mol%) doped congruent $LiNbO_3$ (CLN) single crystals were studied. The exceeding Mg^{2+} doping of 5mol% was found to enhance the dominant red emissions ($^1D_2 \rightarrow {}^3H_4$) under 360nm excitation with a larger population of $^1D_2$ via the Pr^{3+}-Nb^{5+} intervalence charge transfer (IVCT). Quenching of blue-green emissions in Pr^{3+} doped CLNs was ascribed to the depopulation of $^3P_0$ via IVCT state. The lifetimes related to $^1D_2 \rightarrow {}^3H_4$ were significantly increased with Mg^{2+} incorporation at a temperature range from 20K to 430K. As the temperature rises, the progressively thermal quenching of the red emission and lifetime was observed, which was interpreted with the thermally activated energy transfer from the IVCT state to ground level $^3H_4$. More importantly, exceeding Mg^{2+} doping led to a displacement of the IVCT state in the configuration coordinate diagram, resulting in larger quenching activation energy and higher quenching temperature (310K→370K) in Pr:Mg:CLN. The emission enhancement and quenching temperature increase at exceeding Mg^{2+} concentration were considered to be of practical value in luminescent and laser applications.

1. Introduction

In the past decades, the trivalent praseodymium Pr^{3+} offering interesting perspectives as a multifunctional dopant has been intensively investigated. Wide applications have been found in holographic image recording [1], laser emitting [2], fluorescent tubes and scintillators [3,4]. Particular interest was given to the efficient characteristic red emission, with which Pr^{3+} could be applied to white-LEDs for high color rendering index on account of the common deficiency of red component [5]. Prominent red luminescence of high color purity via atypical quenching of blue-green emission had been observed under UV excitation in some Pr^{3+} doped materials [6,7], demonstrating the potential application in displaying and lighting. However, the red luminescence of Pr^{3+} is commonly unstable and inefficient at high temperature [8]. The thermal quenching behavior and low quenching temperature of red emission would prevent the application in high-power optical devices [9,10]. To interpret the blue-green emission quenching and the temperature dependent red emission, the Pr^{3+}-trapped exciton [11] and the metal-to-metal intervalence charge transfer (IVCT) model [12] presenting a low-lying charge transfer state of Pr^{4+}-$M^{(n-1)+}$ (M^{n+}: d^0 electron configured transition metal ions)

#355213 https://doi.org/10.1364/OME.9.001062
Journal © 2019 Received 12 Dec 2018; revised 18 Jan 2019; accepted 20 Jan 2019; published 8 Feb 2019

Optical Materials EXPRESS

had already been proposed, which was consistent with the natural tendency of Pr^{3+} to a tetravalent electronic configuration.

Lithium niobate ($LiNbO_3$) [13] is one of the most widely used multi-functional crystals due to the excellent optical properties and outstanding performance in integrated optics. An overview of the spectroscopic properties in Pr^{3+} doped $LiNbO_3$ ($Pr:LiNbO_3$) had been given by Lorenzo [14] in 1995. Except for applications in holographic recording and compact laser devices, efficient red-emitting piezoluminescence was achieved in $Pr:LiNbO_3$ [15] and the pressure effect on the luminescence properties had been investigated [11] recently. However, to our knowledge, despite the importance of thermal quenching, the temperature dependence of red luminescence in Pr^{3+} doped $LiNbO_3$ is less reported.

The traditional dopant Mg^{2+} is commonly introduced in congruent $LiNbO_3$ (CLN) at threshold (4.6mol% [16]) or exceeding concentration for improving the optical performance, including suppressing photo-damage and enhancing the fluorescence intensity [17,18]. For improving the widespread applications of $LiNbO_3$, 5mol% Mg^{2+} was introduced in the Pr^{3+} doped CLN in our previous work [19]; Long persistent luminescence was achieved in CLN and the essential role of Mg^{2+} incorporation had been demonstrated. However, the research on the influence of Mg^{2+} codoping on red luminescence in Pr:CLN is still insufficient. More importantly, the effect of Mg^{2+} codoping on thermal quenching behavior is worth investigating.

In this paper, based on the detailed spectroscopic characterization of Pr:CLN and Pr:Mg:CLN, the effect of Mg^{2+} codoping on the optical properties of Pr^{3+} in CLN was systematically analyzed. An in-depth analysis of the luminescence mechanism on the frame of the IVCT model was performed based on absorption and luminescence spectra, with which the enhanced red emissions via quenching of blue-green emission could be accounted for. To investigate the difference between the thermal quenching processes, the temperature dependent red emissions and lifetimes related to $^1D_2 \rightarrow {}^3H_4$ in Pr:CLN and Pr:Mg:CLN were studied in detail. The higher quenching temperature of red luminescence in Pr:Mg:CLN would be explained with the configuration coordinate diagram.

2. Experimental

The single crystals Pr:CLN and Pr:Mg:CLN of good quality, as shown in the insets of Fig. 1, were grown along the *c* axis by the Czochralski method. High-purity raw materials (>99.99%) were adopted here. The Pr^{3+} doping contents were intended to be 1mol% in both crystals, while the Mg^{2+} doping content was 5mol% in Pr:Mg:CLN, slightly higher than the threshold concentration. Firstly, the raw materials were mixed well and calcined at 1150°C for the solid-state synthesis of doped CLN polycrystals. Secondly, the polycrystals were melt in a platinum crucible; after seeding the doped CLN single crystals were grown using a homemade automatic control Czochralski puller at a rotating rate of 15rpm and a pulling rate of 1.2mm/h. Finally, the as-grown crystals were cooled to the room temperature at an annealing rate of 10–30°C/h. Wafers oriented perpendicular to and parallel to *c* axis, labeled as σ-polarized and π-polarized, were cut from the central part of the Pr:CLN and Pr:Mg:CLN crystals. The wafers were referred as 1Pr0Mg-σ, 1Pr0Mg-π, 1Pr5Mg-σ and 1Pr5Mg-π respectively hereinafter.

The concentrations of dopants Pr^{3+} and Mg^{2+} in as-grown crystals were estimated by Inductively Coupled Plasma Optical Emission Spectrometry (ICP-OES) with VARIAN-750 type. The Raman spectra under 514.5nm excitation were recorded using a Laser Micro-Raman Spectrometer (Renishaw inVia). The transmission absorption spectra of the wafers were recorded using a UV-Vis-NIR Spectrophotometer (Lambda 950) at room temperature.

The fluorescence excitation spectra, emission spectra and decay curves were recorded by a Photoluminescence Spectrometer (EDINBURGH FLSP920) equipped with a xenon lamp and a microsecond Xe-flash lamp (μF900). The optical signals at the visual (near-infrared) range were detected using a cooled HAMAMATSU RP-928 (R5509-72) photomultiplier tube. For

Optical Materials EXPRESS

the measurements at temperature from 20K to 430K, an ARS closed cycle He refrigerator was used.

3. Results and discussion

3.1 Raman spectra and phonon vibration

The congruent $LiNbO_3$ bulk crystal has a trigonal crystal structure. The concentrations of Pr^{3+} in Pr:CLN and Pr:Mg:CLN were determined to be 1.06 mol% and 1.09 mol%, while the concentration of Mg^{2+} in Pr:Mg:CLN was determined to be 5.21 mol% by the ICP-OES; The effective segregation coefficients were 1.06, 1.09 and 1.04 respectively. The consistent contents of Pr^{3+} and Mg^{2+} in the single crystals and melts verified the successful introduction of the dopants. According to the lithium-vacancy model [20], large amounts of Li-vacancy V_{Li}^{-} and Nb-antisite Nb_{Li}^{4+} distributed in Pr:CLN. In the Pr:Mg:CLN crystal, with the exceeding doping of Mg^{2+}, Nb_{Li}^{4+} was completely eliminated by Mg_{Li}^{+} and excess Mg^{2+} started to replace both normal Li^{+} and Nb^{5+} forming Mg_{Li}^{+} and Mg_{Nb}^{3-} [21]. Pr^{3+} would locate at the normal Li-site and Nb-site since no obvious change could be observed in the Raman tests.

Raman scattering measurements were carried out and the lattice vibrations (phonons) were analyzed. The vibrational modes in Pr:CLN and Pr:Mg:CLN marked in Fig. 1 were consistent with the data of $LiNbO_3$ in previous study [22,23]. The positions of Raman lines appeared to be little affected by exceeding Mg^{2+}-doping. Broadening of Raman lines could be observed in Pr:Mg:CLN especially at 871.68cm^{-1} (E(LO9)), resulting from the formation of new defects Mg_{Li}^{+} and Mg_{Nb}^{3-} and the increased disorder. In both crystals, the energy of the most energetic phonon was 871.68cm^{-1}. So, about 4 phonons of this type were needed to bridge the gap (about 3592cm^{-1}) between $^3P_0$ and $^1D_2$ of Pr^{3+}, while the gap (about 6619cm^{-1}) between $^1D_2$ and $^1G_4$ would take about 8 phonons, indicating that the multi-phonon relaxation between $^1D_2$ and $^1G_4$ was relatively inefficient.

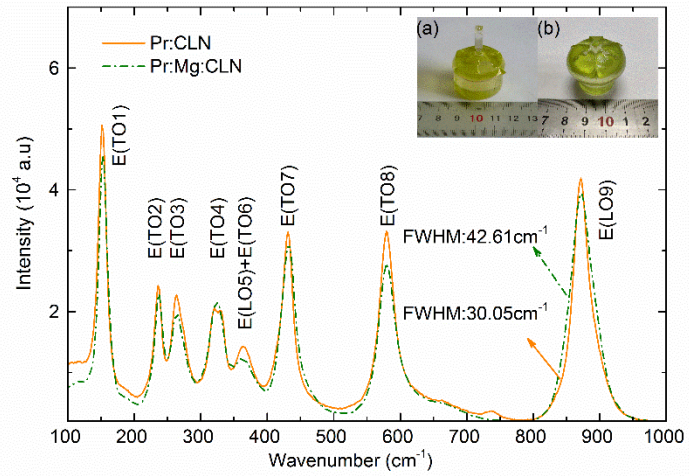

Fig. 1. Raman spectra of Pr^{3+} doped and Pr^{3+}-Mg^{2+} codoped congruent $LiNbO_3$ crystals (Pr:CLN and Pr:Mg:CLN), with the photographs displaying the appearance of the as-grown single crystals (a) Pr:CLN and (b) Pr:Mg:CLN in the insets.

3.2 Absorption spectra

The transmission absorption spectra of the wafers 1Pr0Mg-σ, 1Pr0Mg-π, 1Pr5Mg-σ and 1Pr5Mg-π at wavelength range from 350nm to 2500nm were presented in Fig. 2.

Optical Materials EXPRESS

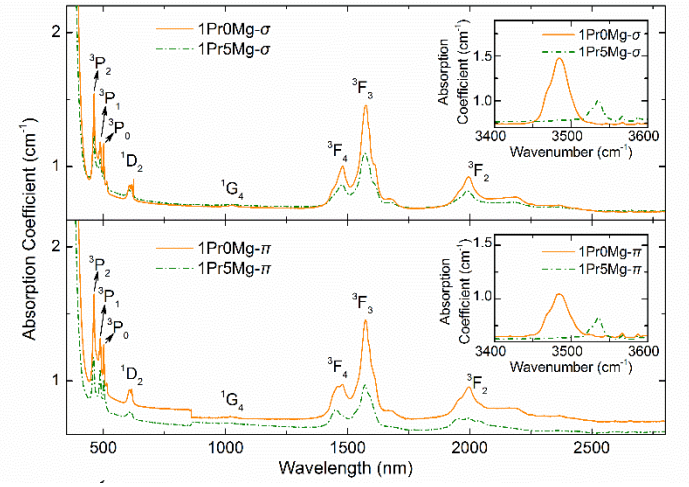

Fig. 2. The polarized transmittance absorption spectra of Pr:CLN and Pr:Mg:CLN wafers, referred as 1Pr0Mg-σ, 1Pr0Mg-π, 1Pr5Mg-σ and 1Pr5Mg-π, at the wavelength range from 350nm to 2500nm. In the insets: the infrared absorption spectra at around 3500cm^{-1} (2857nm).

The spectra consisted of absorption bands corresponding to the transitions of Pr^{3+} from ground level $^3H_4$ to excited levels $^3P_0$, $^3P_1$, $^3P_2$, $^1D_2$, $^1G_4$, $^3F_4$, $^3F_3$ and $^3F_2$. There was an apparent decrease in the absorption coefficient after 5mol% Mg^{2+}-doping, revealing that the efficiencies of the 4*f*-4*f* absorption transitions decreased in Pr:Mg:CLN. This could be partially explained with the less polarizable chemical environment [24,25] in Pr:Mg:CLN when all intrinsic defects were eliminated. According to the equations of Judd-Ofelt theory, there would be a decrease in the efficiencies of both the 4*f*-4*f* absorption (η_{ap}) and emission (η_{em}) transitions in Pr:Mg:CLN.

The infrared absorption spectra at around 3500cm^{-1} (2857nm) of Pr:CLN and Pr:Mg:CLN were presented in the insets of Fig. 2. Evident violet shift of the absorption peak related to the OH^- absorption could be observed after Mg^{2+} codoping.

3.3 Luminescence spectra and mechanism analysis

The fluorescence excitation spectra of the four wafer samples monitored at 618nm were measured and depicted in Fig. 3 (a) and (d). Except for the excitation peaks centered at 462nm 489nm and 501nm associated with the excited levels $^3P_2$ $^3P_1$ and $^3P_0$ ($^3P_{2\text{-}0}$), broad excitation bands at around 360nm were observed in all wafers. The 360nm excitation bands were very close to the absorption edge, which was determined to be 349.6nm (325.10nm) in Pr:CLN (Pr:Mg:CLN) based on absorption spectra, and located in the strong fundamental absorption region of CLN; It was hard to identify them in the absorption spectra. The wide excitation bands could not be assigned to any 4*f*-4*f* transition and would be attributed to the transition from ground level $^3H_4$ to the IVCT state according to the IVCT model. After doping with 5mol% Mg^{2+}, no evident changes were found on the $^3P_{2\text{-}0}$ excitation bands. However, the IVCT excitation bands extended to shorter wavelength from 300nm to 250nm in 1Pr5Mg-σ and 1Pr5Mg-π, resulting in changes of spectra in appearance. The extension was supposed to be related to a slight elevation of the IVCT state after exceeding Mg^{2+} doping.

Optical Materials EXPRESS

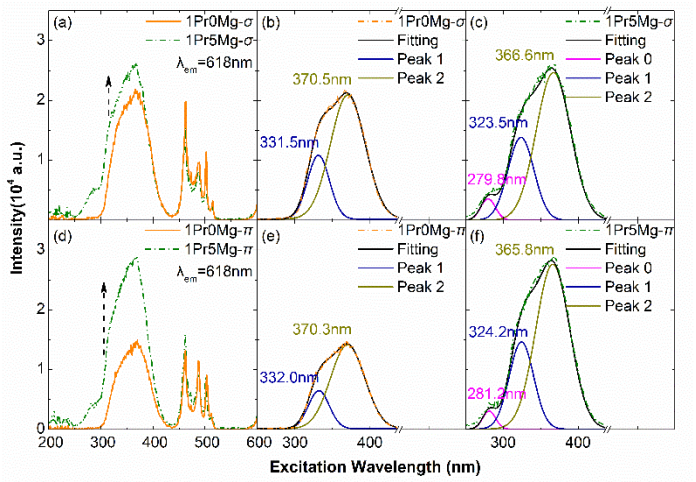

Fig. 3. The (a) σ-polarized (d) π-polarized fluorescence excitation spectra measured by monitoring 618nm emissions in Pr:CLN and Pr:Mg:CLN. The Gaussian decomposition of the excitation band from 250nm to 450nm in (b) 1Pr0Mg-σ (c) 1Pr5Mg-σ (e) 1Pr0Mg-π (f) 1Pr5Mg-π, with the central wavelengths of Gauss peaks Peak0 Peak1 and Peak2 marked beside.

For further insight of the excited levels related to the broad excitation band, the excitation bands from 250nm to 450nm in1Pr0Mg-σ 1Pr5Mg-σ 1Pr0Mg-π and 1Pr5Mg-π were decomposed into Gauss peaks, as presented in Fig. 3 (b) (c) (e) and (f). An extra Gauss peak Peak0 centered at around 280nm was observed only in Pr:Mg:CLN. Peak0 might be attributed to a transition related to the new defect levels introduced by Mg^{2+} incorporation, which had been demonstrated to be essential for the occurrence of long persistence luminescence in Pr:Mg:CLN [19]. Besides, the Peak1 and Peak2 could be found in all 4 wafers and might be attributed to the transition from $^3H_4$ to IVCT level. With the violet shift of Peak1 and Peak2, we confirmed a slight elevation of the IVCT state in Pr:Mg:CLN.

Higher intensities of 360nm excitation bands were also detected in Pr:Mg:CLN. Accordingly, the main red emissions ($^1D_2 \rightarrow {}^3H_4$ of Pr^{3+}) under 360nm excitation were stronger in 1Pr5Mg-σ and 1Pr5Mg-π respectively compared to those in Pr0Mg-σ and 1Pr0Mg-π, as presented in Fig. 4 (a) and (b). Since the emission spectra were all measured under the same circumstances, higher luminescence efficiency P_{Lum} related to the transition $^1D_2 \rightarrow {}^3H_4$ under 360nm excitation was achieved after exceeding Mg^{2+} doping.

Optical Materials EXPRESS

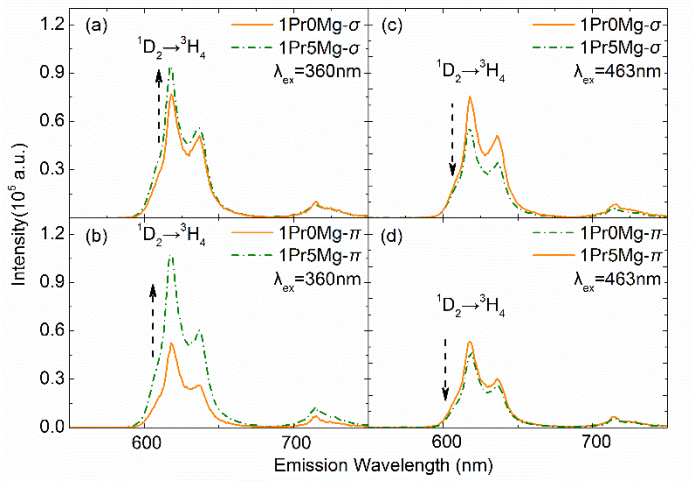

Fig. 4. The (a) σ-polarized (b) π-polarized fluorescence emission spectra recorded under 360nm excitation. The (c) σ-polarized (d) π-polarized fluorescence emission spectra recorded under 463nm excitation.

In principle, the luminescence efficiency P_{lum} should be positively associated with the feeding probability via IVCT (P_{IVCT}) and the 4*f*-4*f* transition efficiency η_{em}, expressed as: $P_{Lum} \propto P_{IVCT} \times \eta_{em}$. To confirm the decrease of η_{em} in Pr:Mg:CLN, fluorescence emission spectra under 463nm excitation were measured and depicted in Fig. 4(c) and (d). When excited with 463nm incident ray, Pr^{3+} could only be excited to 4*f* levels $^3P_{2\text{-}0}$. The excited Pr^{3+} in $^3P_{2\text{-}1}$ would relax to the nearby lower level $^3P_0$ promptly via multi-phonon relaxation and then relax to $^1D_2$ via a nonradiative process, followed by efficient red emissions at 618nm. This route was less related to the IVCT state. The emission efficiency and intensity under 463nm excitation were mainly associated with η_{em}. The slightly reduced 618nm emission intensities in 1Pr5Mg-σ and 1Pr5Mg-π compared to those in 1Pr0Mg-σ and 1Pr0Mg-π indicated a lower 4*f*-4*f* transition efficiency η_{em} when doped with 5mol% Mg^{2+}. This observation coincided with the changes in absorption spectra in Section 3.2. With the increasing P_{Lum} and decreasing η_{em}, we concluded that the feeding probability to $^1D_2$ via IVCT P_{IVCT} increased with exceeding Mg^{2+} doping.

An configuration coordinate diagram which could offer great convenience for the explanation of the IVCT-based luminescent mechanism in Pr:CLN and Pr:Mg:CLN was constructed and depicted in Fig. 5. The configurational coordinate diagram was based on the breathing model of optical center (Pr^{3+} and its ligands ions) [26]. The parabolas here represented the Pr^{3+}-Nb^{5+} IVCT state and the different energy states of the optical center, including Pr^{3+} in different 4*f* levels and the vibration energy of the ligands. The positions of all parabolas were determined based on the data from luminescence and absorption spectra.

Two mechanisms for red emissions were presented in Fig. 5. Under 360nm excitation, charge transfer occurred from Pr^{3+} to $4d^0$ orbit of Nb^{5+} and Pr^{3+} was excited into IVCT state, followed by de-excitation directly to $^1D_2$ bypassing the levels $^3P_{2\text{-}0}$. Under 463nm excitation, Pr^{3+} reached the excited levels $^3P_{2\text{-}0}$ and then de-excited to $^1D_2$ via the crossovers between the IVCT state and levels $^3P_{2\text{-}0}$ or $^1D_2$. The energy barriers were low and the IVCT state could work as an effective quenching channel for $^3P_{2\text{-}0}$ in both crystals. So in all our samples, the characteristic blue-green emissions at around 500nm related to transition $^3P_0 \rightarrow {}^3H_4$ were almost completely quenched. Only 618nm and 715nm emissions from excited level $^1D_2$ could be found in Fig. 4.

Optical Materials EXPRESS

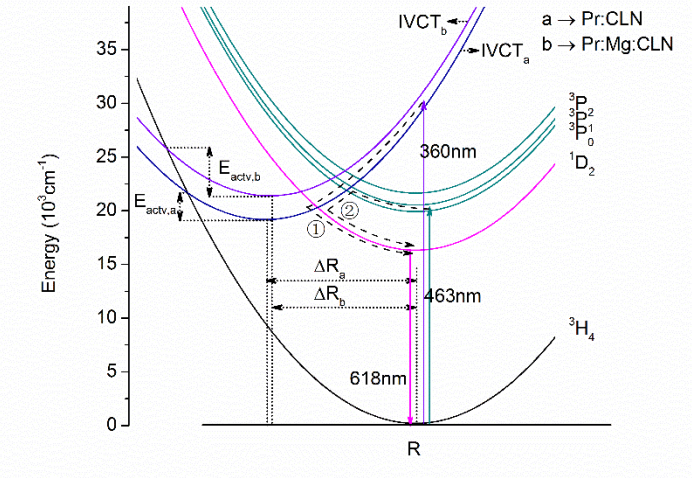

Fig. 5. The configurational coordinate diagram of Pr:CLN and Pr:Mg:CLN, depicting the light-emitting mechanism based on the intervalence charge transfer. IVCT$_i$ (i = a, b) represented the Pr^{3+}–Nb^{5+} intervalence charge transfer state; $E_{actv,i}$ represented the quenching activation energy; ΔR_i represented the coordinate offset of IVCT state; Dashed arrows ① and ② signified the quenching of $^3P_0$ emissions under ① 360nm excitation and ② 463nm excitation.

3.4 Temperature quenching of red emissions and lifetimes related to $^1D_2 \rightarrow {}^3H_4$

The unpolarized fluorescence emission spectra of Pr:CLN and Pr:Mg:CLN under 360nm excitation were recorded at the temperature ranging from 20K to 430K, as presented in Fig. 6 (a) and (b). As temperature increased, the normalized intensity I of the red emission weakened slowly at first but then faster and faster. The decrease of intensity ratio I/I_{0K} was also pronounced at higher temperatures as depicted in Fig. 6 (c). The inflexions of the ratio curves were found at around 250K, followed by a sharp drop and finally quenching of red emissions. Noteworthily, compared to Pr:CLN, the intensity ratio in Pr:Mg:CLN decreased less quickly with smaller curvature.

The quenching at higher temperatures was caused by the thermally activated energy transfer from IVCT state to ground level $^3H_4$ of Pr^{3+}. With temperature rising, the electrons on the bottom of IVCT state could more easily migrate to its crossover with $^3H_4$ and then relax there, bypassing and depopulating $^1D_2$.

Optical Materials EXPRESS

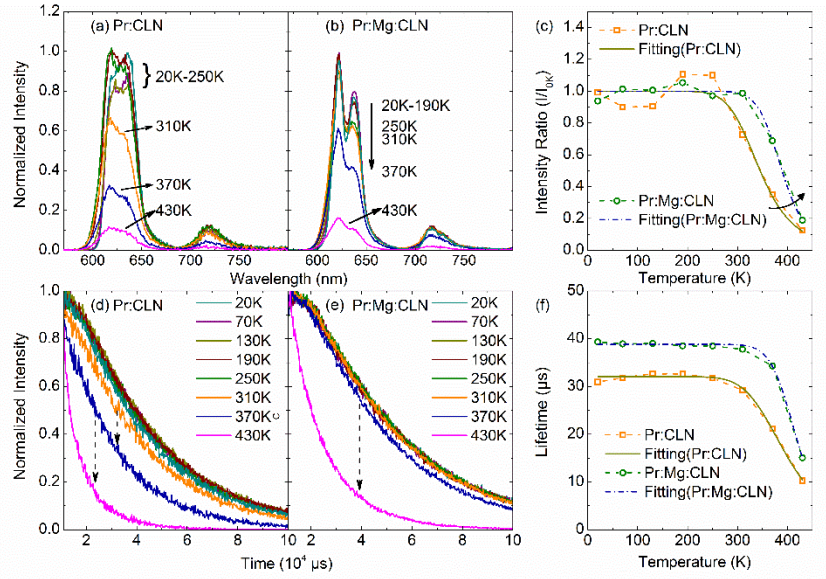

Fig. 6. The normalized temperature-dependent fluorescence emission spectra at temperatures ranging from 20K to 430K under 360nm excitation in (a) Pr:CLN and (b) Pr:Mg:CLN. (c) The temperature dependences of emission intensity ratio I/I_{0K} related to the transition $^1D_2 \rightarrow {}^3H_4$ and the fitting curves acquired using formula (1). The temperature-dependent fluorescence decay curves from excited level $^1D_2$ measured under 360nm excitation in (d) Pr:CLN and (e) Pr:Mg:CLN. (f) The temperature dependences of the radiant lifetime and the fitting curves acquired using formula (1).

Further analysis on the difference between the temperature dependence of fluorescence in Pr:CLN and that in Pr:Mg:CLN could be carried out according to the theory put forward by Struck [8,27]. The temperature-dependent red emission data could be reliably fitted by the formula:

$$I(T)/I_{0K} = [1 + A\exp(-E_{actv}/k_B T)]^{-1} \quad (1)$$

where I_{0K} represents the emission intensity at 0K; A is a pre-exponential constant; k_B is the Boltzmann constant; The quenching activation energy E_{actv}, representing the vertical distance from the minimum of IVCT state to its crossover with the quenching level in the coordinate diagram [28], is correlated to the probability of the temperature-dependent nonradiative relaxation [26]. The fitting curves were also presented in Fig. 6 (c). The indicative value of E_{actv} was determined to be 2420.07cm^{-1} in Pr:CLN and 4134.97cm^{-1} in Pr:Mg:CLN. Despite only eight sampling temperatures and consequently relative low accuracy of E_{actv}, we could draw a qualitative conclusion that the red emissions tended to be quenched more difficultly due to the higher energy barrier in Pr:Mg:CLN.

The decay curves related to the $^1D_2 \rightarrow {}^3H_4$ transition from 20K to 430K were measured under 360nm excitation and presented in Fig. 6 (d) and (e). All the decay curves exhibited a single exponential behavior. The values of lifetime were determined and plotted in Fig. 6 (f). The lifetime values of Pr:CLN at low temperatures were consistent with the data reported in [14]. With exceed Mg^{2+} doping, the lifetimes in Pr:Mg:CLN at the temperature from 20K to 430K were significantly increased. The increased lifetime of red emission after Mg^{2+}-codoping agreed with the increasing radiative lifetime of excited level $^1D_2$, which would result from the lower transition probabilities as discussed in Section 3.2 and 3.3.

The temperature dependences of the lifetime and those of emission intensity related to $^1D_2 \rightarrow {}^3H_4$ were interrelated. As temperatures rose, the reduction of lifetime became more and more apparent, following the same tendency of intensity variation. Similarly, the E_{actv} could

Optical Materials EXPRESS

be also calculated from the lifetime data. The fitting curves were presented in Fig. 6 (f). The values of E_{actv} were 2486.79cm^{-1} and 4519.52cm^{-1} for Pr:CLN and Pr:Mg:CLN respectively. Moreover, according to the fitting results, it was obvious that the more accurate way to determine E_{actv} was to measure the lifetimes rather than emission intensities; the latter could be more easily influenced by environmental disturbances and absorption strength change with temperature.

The reason for higher E_{actv} in Pr:Mg:CLN was illustrated in Fig. 5. Firstly, the extension to shorter wavelength of the IVCT-related excitation band mentioned above vertically elevated the corresponding IVCT parabola and increased E_{actv}. Secondly, the smaller coordinate offset of IVCT state (ΔR), which represented the distance between ligand and central ion Pr^{3+}, was also responsible. When doping with exceeding Mg^{2+} ions, excess Mg^{2+} would partially locate at normal Nb-site according to the Li-vacancy model. Due to the larger diameter of Mg^{2+} than Nb^{5+}, the substitution would enlarge the lattice environment in the vicinity of Mg_{Nb}^{3-}. Supposing that there was also Pr_{Li}^{2+} in the vicinity, it was reasonable to infer that the lattice environment of Pr_{Li}^{2+} and the nearest Nb^{5+} shrank. With smaller ΔR, the IVCT parabola of Pr:Mg:CLN shifted right, inducing a further increase of E_{actv}.

As a practical matter, the heating effect caused by the strong absorption of excitation light would raise the temperature of crystals. Consequently, the relative low quenching temperature of 310K (36.85°C), at which precipitous quenching for red-emission intensities and lifetimes in Pr:CLN started to occur, would limit the applications in luminescent/laser devices. It was noteworthy that the higher quenching temperature of 370K (96.85°C) was achieved in Pr:Mg:CLN, which was of practical value in luminescent or laser applications. Besides, the temperature dependences of Pr^{3+} doped CLNs from 275K to 400K could be tuned with Mg^{2+} dopant. The temperature sensitivities offered interesting prospects for use in temperature sensors and deserved a further investigation.

4. Conclusion

The effect of exceeding Mg^{2+} doping on the optical properties of Pr^{3+} in CLN has been investigated based on the absorption, excitation and emission spectra. Blue-green emissions were quenched completely in CLN due to the depopulation of $^3P_0$ via IVCT state. The exceeding Mg^{2+} doping was found to reduce the red emission excited at 463nm indicating the decrease of 4f-4f transition probability, but enhance the one excited at 360nm due to the larger population of $^1D_2$ via IVCT. The temperature-dependent red emissions and lifetimes under 360nm excitation were measured. The lifetimes from 20K to 430K related to $^1D_2 \rightarrow {}^3H_4$ were significantly increased by the Mg^{2+} incorporation. Thermal quenching for red light emission and lifetime in Pr:CLN and Pr:Mg:CLN was demonstrated to be caused by thermally activated energy transfer from IVCT state to $^3H_4$ of Pr^{3+}. The quenching temperature was found to be raised by the exceeding Mg^{2+} doping, which was meaningful in actual luminescent and laser application. The quenching activation energy was calculated and higher energy barrier for quenching in Pr:Mg:CLN was interpreted considering the displacement of the IVCT state in configurational coordinate diagram. Besides, the temperature sensitivities and the tunability by Mg^{2+} doping in Pr^{3+} doped CLN were regarded to be of practical value in sensor applications. This work is considered to be promotive for understanding the luminescence mechanism based on IVCT process in Pr^{3+} doped materials.

Funding

National Natural Science Foundation of China (NSFC) (Nos. 11302268, 11372361, 11832019, 11472313, 11572355); the Natural Science Foundation of Guangdong province (2018A030313909); the Guangdong Science & Technology Project (2015B090927005).

Optical Materials EXPRESS

References

1. Y. S. Bai, R. R. Neurgaonkar, and R. Kachru, "High-efficiency nonvolatile holographic storage with two-step recording in praseodymium-doped lithium niobate by use of continuous-wave lasers," Opt. Lett. **22**(5), 334–336 (1997).
2. P. W. Metz, F. Reichert, F. Moglia, S. Müller, D. T. Marzahl, C. Kränkel, and G. Huber, "High-power red, orange, and green Pr^{3+}:$LiYF_4$ lasers," Opt. Lett. **39**(11), 3193–3196 (2014).
3. J. Pejchal, M. Nikl, E. Mihokova, J. A. Mares, A. Yoshikawa, H. Ogino, K. M. Schillemat, A. Krasnikov, A. Vedda, K. Nejezchleb, and V. Mucka, "Pr^{3+}-doped complex oxide single crystal scintillators," J. Phys. D Appl. Phys. **42**(5), 055117 (2009).
4. T. Yanagida, "Ionizing radiation induced emission: Scintillation and storage-type luminescence," J. Lumin. **169**, 544–548 (2016).
5. L. L. Zhang, J. H. Zhang, X. Zhang, Z. D. Hao, G. H. Pan, and H. J. Wu, "Site distortion in Li_2SrSiO_4: Influence on Pr^{3+} emission and application in wLED," J. Lumin. **180**, 158–162 (2016).
6. P. Boutinaud, E. Pinel, M. Dubois, A. P. Vink, and R. Mahiou, "UV-to-red relaxation pathways in $CaTiO_3$: Pr^{3+}," J. Lumin. **111**(1–2), 69–80 (2005).
7. S. Zhang, H. Liang, C. Liu, Z. Qi, T. Shao, and Y. Wang, "High color purity red-emission of $NaGdTiO_4$:Pr^{3+} via quenching of $^3P_0$ emission under low-voltage cathode ray excitation," Opt. Lett. **38**(5), 612–614 (2013).
8. C. W. Struck and W. H. Fonger, "Thermal quenching of Tb^{3+}, Tm^{3+}, Pr^{3+}, and Dy^{3+} $4f^n$ emitting states in La_2O_2S," J. Appl. Phys. **42**(11), 4515–4516 (1971).
9. K. Fiaczyk, S. Omagari, A. Meijerink, and E. Zych, "Temperature dependence of $4f^{n-1}5d^1$-> $4f^n$ luminescence of Ce^{3+} and Pr^{3+} ions in Sr_2GeO_4 host," J. Lumin. **198**, 163–170 (2018).
10. F. B. Xiong, H. F. Lin, Y. C. Xu, H. X. Shen, and W. Z. Zhu, "New thermally stable red-emitting phosphors Pr^{3+}, M^+:SrB_4O_7 (M=Li, Na, K)," J. Lumin. **177**, 99–103 (2016).
11. W. Gryk, C. Dujardin, M. F. Joubert, W. Ryba-Romanowski, M. Malinowski, and M. Grinberg, "Pressure effect on luminescence dynamics in Pr^{3+}-doped $LiNbO_3$ and $LiTaO_3$ crystals," J. Phys. Condens. Matter **18**(1), 117–125 (2006).
12. P. Boutinaud, E. Pinel, M. Oubaha, R. Mahiou, E. Cavalli, and M. Bettinelli, "Making red emitting phosphors with Pr^{3+}," Opt. Mater. **28**(1–2), 9–13 (2006).
13. B. T. Matthias and J. P. Remeika, "Ferroelectricity in the Ilmenite Structure," Phys. Rev. **76**(12), 1886–1887 (1949).
14. A. Lorenzo, L. E. Bausá, and J. Garcia Sole, "Optical spectroscopy of Pr^{3+} ions in $LiNbO_3$.," Phys. Rev. B Condens. Matter **51**(23), 16643–16650 (1995).
15. D. Tu, C. N. Xu, A. Yoshida, M. Fujihala, J. Hirotsu, and X. G. Zheng, "$LiNbO_3$:Pr^{3+} : A Multipiezo Material with Simultaneous Piezoelectricity and Sensitive Piezoluminescence," Adv. Mater. **29**(22), 1606914 (2017).
16. D. A. Bryan, R. Gerson, and H. E. Tomaschke, "Increased optical damage resistance in lithium niobate," Appl. Phys. Lett. **44**(9), 847–849 (1984).
17. P. X. Zhang, J. G. Yin, L. H. Zhang, Y. C. Liu, J. Q. Hong, K. J. Ning, Z. Chen, X. Y. Wang, C. J. Shi, and Y. Hang, "Efficient enhanced 1.54 μm emission in Er/Yb: $LiNbO_3$ crystal codoped with Mg^{2+} ions," Opt. Mater. **36**(12), 1986–1990 (2014).
18. L. Xing, W. Yang, J. Lin, M. Huang, and Y. Xue, "Enhanced and Stable Upconverted White-light Emission in Ho^{3+}/Yb^{3+}/Tm^{3+}-doped $LiNbO_3$ Single Crystal via Mg^{2+} Ion Doping," Sci. Rep. **7**(1), 14725 (2017).
19. P. L. Shao, W. X. Chen, D. C. Ma, S. L. Hua, S. W. Long, and B. Wang, "Persistent luminescence found in Mg^{2+} and Pr^{3+} co-doped $LiNbO_3$ single crystal," J. Mater. Chem. C Mater. Opt. Electron. Devices **6**(37), 10067–10072 (2018).
20. P. Lerner, C. Legras, and J. P. Dumas, "Stoechiométrie des monocristaux de métaniobate de lithium," J. Cryst. Growth **3–4**, 231–235 (1968).
21. R. Mouras, M. D. Fontana, P. Bourson, and A. V. Postnikov, "Lattice site of Mg ion in $LiNbO_3$ crystal determined by Raman spectroscopy," J. Phys. Condens. Matter **12**(23), 5053–5059 (2000).
22. V. Caciuc, A. V. Postnikov, and G. Borstel, "Ab initio structure and zone-center phonons in LiNbO3," Phys. Rev. B Condens. Matter Mater. Phys. **61**(13), 8806–8813 (2000).
23. P. Hermet, M. Veithen, and P. Ghosez, "First-principles calculations of the nonlinear optical susceptibilities and Raman scattering spectra of lithium niobate," J. Phys. Condens. Matter **19**(45), 456202 (2007).
24. Y. N. Qian, R. Wang, C. Xu, X. H. Wu, L. L. Xing, and Y. L. Xu, "Optical spectroscopy and laser parameters of Zn^{2+}/Er^{3+}/Yb^{3+}-tridoped $LiNbO_3$ crystal," J. Lumin. **132**(8), 1976–1981 (2012).
25. A. Li, L. Sun, Z. Zheng, W. Wu, W. Liu, Y. Yang, T. Lu, and W. Su, "Spectroscopic analysis of Er^{3+} transition in Mg/Er-codoped $LiNbO_3$ crystal," J. Lumin. **128**(2), 239–244 (2008).
26. C. Y. Shang, X. H. Shang, Y. Q. Qu, and M. C. Li, "Quenching mechanisms of the optical centers in Eu^{3+}-doped nanophosphors under charge transfer excitation," J. Appl. Phys. **108**(9), 094328 (2010).
27. M. D. Chambers, P. A. Rousseve, and D. R. Clarke, "Decay pathway and high-temperature luminescence of Eu^{3+} in $Ca_2Gd_8Si_6O_{26}$," J. Lumin. **129**(3), 263–269 (2009).
28. Y. Gao, F. Huang, H. Lin, J. C. Zhou, J. Xu, and Y. S. Wang, "A Novel Optical Thermometry Strategy Based on Diverse Thermal Response from Two Intervalence Charge Transfer States," Adv. Funct. Mater. **26**(18), 3139–3145 (2016).